

# Mode-Interference-Induced Chiral Exceptional Points in Momentum Space

Xi Zhao, Zhancheng Li,\* Guangzhou Geng, Wenwei Liu, Jiaqi Cheng, Hua Cheng,\* and Shuqi Chen\*

Non-Hermitian metasurfaces with chiral exceptional points (EPs) in their scattering matrices have garnered significant attention due to their potential for optical polarization manipulation and wavefront control. However, existing approaches predominantly operate under normal incidence conditions, limiting their application in the manipulation of chiral EPs in momentum space. Here, the wavelength-fixed manipulation of the chiral EPs across a wide-range momentum space using a polyatomic metasurface is realized, which is attributed to the effective modulation of the collective interference of guided-mode resonances excited by oblique transverse magnetic (TM) and transverse electric (TE) illuminations. Further, both theoretical and experimental analyses are conducted to explore the potential applications of the proposed design in the wavevector- and spin-selective manipulation of reflection intensity and optical encryption. This work provides a straightforward method to realize and manipulate chiral EPs in momentum space at a fixed operational wavelength, paving the way for designing polarization-selective and wavevector-selective devices.

## 1. Introduction

The exceptional points (EPs) are branching singularities in the parameter space at which two or more eigenvalues and the corresponding eigenvectors degenerate simultaneously.<sup>[1–4]</sup> The EPs have been observed in various open classical or quantum systems, such as particle-diffusion system, electromagnetism, condensed exciton-polaritons, as well as acoustics.<sup>[5–9]</sup> In the field of optical and photonic systems, EPs have been extensively studied in optical microcavity, optical waveguides, fiber loops, and photonic crystal slabs.<sup>[10–16]</sup> EPs can significantly affect the response of the photonic system due to the abrupt phase transitions in the eigenvalue spectrum, which have been shown to lead to many interesting phenomena, such as chiral state transfer,<sup>[17,18]</sup> unidirectional propagation,<sup>[19,20]</sup> topological

chirality,<sup>[21,22]</sup> EP pair,<sup>[23]</sup> laser mode selection,<sup>[24,25]</sup> and loss-induced transparency.<sup>[26]</sup> Scattering EPs are EPs of scattering matrices, which is one of the representative phenomena of the investigated advancements of EPs.<sup>[27]</sup> Generally speaking, the optical scattering behavior of typical optical systems can be characterized by using the scattering matrices in complex parameter space.<sup>[28–30]</sup> When the scattering EPs happen, the eigenvalue splitting disappears and the associated scattering matrix becomes defective.<sup>[31–35]</sup> To realize the scattering EPs, the precise modulation of the coefficients of the scattering matrix is necessary.

Metasurfaces, artificial 2D arrays composed of subwavelength-sized structures, provide an ideal platform for the exploration of the physics and functionality of scattering EPs, since the coefficients of their scattering matrices can be flexibly tailored.<sup>[36,37]</sup> The chiral EPs appear with a single circularly polarized transmission or reflection eigenstate of the scattering matrix, possessing a well-defined inherent chirality for the system within the parameter space. For the construction of chiral EPs based on metasurfaces, polyatomic metasurfaces have an edge over monoatomic metasurfaces, which offer more design degrees of freedom to tune the near-field coupling between optical resonators in each unit cell of metasurfaces, resulting in the degeneracy of eigenvalues of the scattering matrices.<sup>[38–41]</sup> Some intriguing achievements of chiral EPs based on the polyatomic metasurfaces platform have been reported.<sup>[28,29,40,41]</sup> Kang et al. demonstrated the

X. Zhao, Z. Li, W. Liu, J. Cheng, H. Cheng, S. Chen  
The Key Laboratory of Weak Light Nonlinear Photonics  
Ministry of Education  
School of Physics and TEDA Institute of Applied Physics  
Nankai University  
Tianjin 300071, China  
E-mail: [zcli@nankai.edu.cn](mailto:zcli@nankai.edu.cn); [hcheng@nankai.edu.cn](mailto:hcheng@nankai.edu.cn);  
[schen@nankai.edu.cn](mailto:schen@nankai.edu.cn)

G. Geng  
Beijing National Laboratory for Condensed Matter Physics  
Institute of Physics  
Chinese Academy of Sciences  
Beijing 100190, China

S. Chen  
School of Materials Science and Engineering  
Smart Sensing Interdisciplinary Science Center  
Nankai University  
Tianjin 300350, China

S. Chen  
The Collaborative Innovation Center of Extreme Optics  
Shanxi University  
Taiyuan, Shanxi 030006, China

 The ORCID identification number(s) for the author(s) of this article can be found under <https://doi.org/10.1002/lpor.202301257>

DOI: 10.1002/lpor.202301257

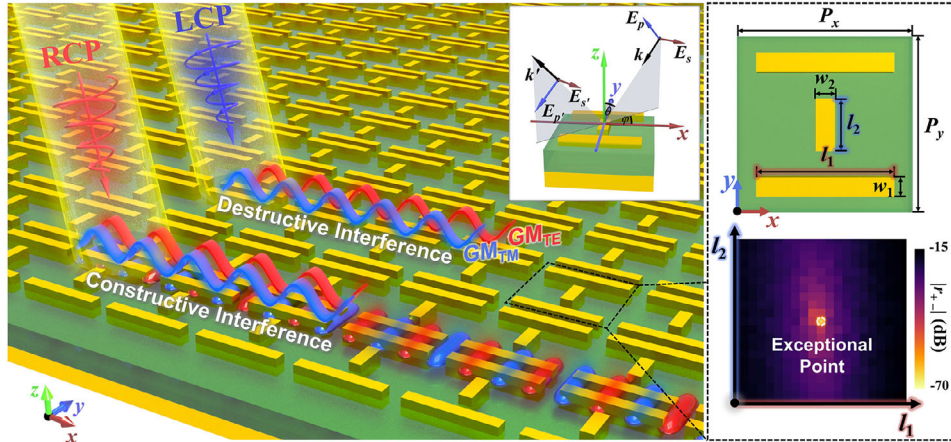


**Figure 1.** Schematic of the designed polyatomic metasurface for the manipulation of chiral EP in momentum space. The interference between the guided-mode resonances under TE and TM oblique illuminations can be effectively manipulated by adjusting the length parameters  $l_1$  and  $l_2$ , resulting in the controllable reflection coefficient  $r_{+-}$ . The chiral EPs can be achieved within the parameter space defined by these two length parameters, which can be manipulated across a wide-range momentum space while maintaining a consistent operational wavelength. Inset: definition of the incident angle.

realization of chiral EPs on a metasurface by tuning the coupling and losses rates of the pair of linear resonators in each unit cell.<sup>[29]</sup> Song et al. proposed a fresh phase-addressing retardation mechanism by engineering a topologically protected full-phase accumulation surround a chiral EP on a specific reflected polarization regime.<sup>[41]</sup> These approaches demonstrate the significant potential of chiral EP for manipulating optical waves. However, until now, the implementation of chiral EPs has mostly occurred under normal incidence. A viable strategy for the implementation and manipulation of chiral EP in momentum space, which could significantly broaden their applications, has yet to be presented.

Here, we propose an effective approach for manipulating chiral EPs across a wide range of momentum space by strategically modulating the collective interference between guided-mode resonances (GMRs) within a polyatomic metasurface. The proposed metasurface composed of two types of gold nanorods can form the GMRs for both oblique transverse magnetic (TM) and transverse electric (TE) illuminations, whose field distributions are similar, indicating the excitation of the same resonance mode. The collective interference of these GMRs can be effectively modulated by adjusting the lengths of the nanorods, resulting in chiral EPs that can be manipulated across a wide momentum space while maintaining a fixed operational wavelength. Our work provides a straightforward method to realize and manipulate the chiral EPs in momentum space. The potentialities of the proposed design for spin-selective manipulation of reflection intensity and optical encryption have also been theoretically and experimentally validated.

## 2. Results and Discussion

A schematic illustration of the designed metasurface for the manipulation of chiral EPs in momentum space, is illustrated in **Figure 1**. It is a typical metal/insulator/metal design, in which a  $\text{SiO}_2$  interlayer is sandwiched between a ground gold layer and a structured gold layer, and a SU-8 capping layer stacked vertically on the top of the MIM structure. The thicknesses of the struc-

tured gold layer, the  $\text{SiO}_2$  interlayer, and the ground gold layer are set as  $t_1 = 30$  nm,  $t_2 = 130$  nm, and  $t_3 = 95$  nm, respectively. The thickness of the SU-8 capping layer is set as 126 nm. The structured gold layer is made up of two types of rectangular gold nanorods whose lengths and widths are  $l_1 = 520$  nm,  $w_1 = 70$  nm and  $l_2 = 175$  nm,  $w_2 = 75$  nm. The distance between the two long nanorods is  $d = 430$  nm, and the period of the unit cell in the  $x$  and  $y$  directions are  $P_x = P_y = 560$  nm. Here, the proposed metasurface is used for the realization of chiral EP in the reflection regime. All of our analyses are based on a given Cartesian coordinate system, as illustrated in the inset of **Figure 1**. The wave vector of incident light is defined by two angles ( $\theta, \varphi$ ).  $\theta$  is defined as the angle between the oblique wave vector and the  $z$ -axis, while  $\varphi$  is defined as the angle between the projection of the oblique wave vector onto the  $x$ - $y$  plane and the  $x$ -axis. Here, we defined the parameter-dependent reflection matrix of the designed metasurface in the linear polarization basis as:

$$\mathbf{R}_{\text{lin}} = \begin{bmatrix} r_{pp} & r_{ps} \\ r_{sp} & r_{ss} \end{bmatrix} \quad (1)$$

where the subscripts “ $i$ ” and “ $j$ ” of  $r_{ij}$  represent the polarization state of the reflected and incident wave respectively. The relationship between the oblique incident ( $a_i$ ) and reflected ( $b_i$ ) plane waves can be expressed as  $[b_p, b_s]^T = \mathbf{R}_{\text{lin}}[a_p, a_s]^T$ . The subscript “ $i$ ” of  $a_i$  and  $b_i$  indicate the linearly polarization state of the incident and reflected waves. By changing the base vectors into circularly polarization basis  $(1, \pm i)/\sqrt{2}$  and defining “+” and “-” to represent clockwise and counter-clockwise spins when observed from the  $-z$  direction, the reflection matrix can be rewritten as:

$$\begin{aligned} \mathbf{R}_{\text{circ}} &= \begin{bmatrix} r_{++} & r_{+-} \\ r_{-+} & r_{--} \end{bmatrix} \\ &= \frac{1}{2} \begin{bmatrix} r_{pp} + r_{ss} + i(r_{ps} - r_{sp}) & r_{pp} - r_{ss} - i(r_{ps} + r_{sp}) \\ r_{pp} - r_{ss} + i(r_{ps} + r_{sp}) & r_{pp} + r_{ss} - i(r_{ps} - r_{sp}) \end{bmatrix} \end{aligned} \quad (2)$$

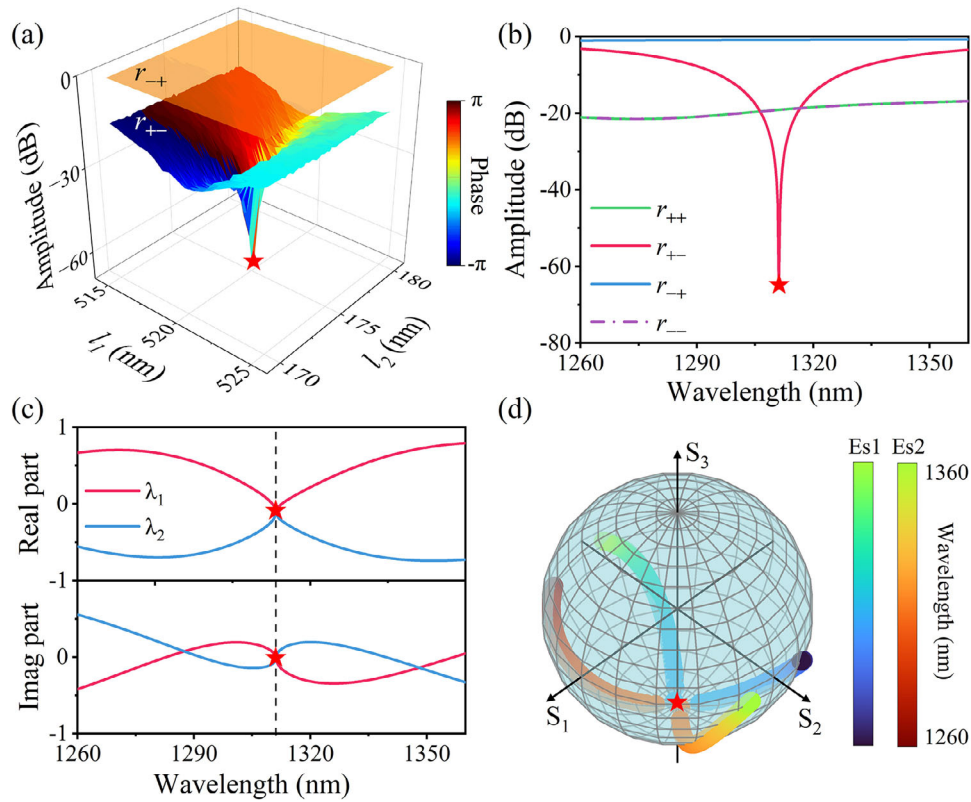


**Figure 2.** Implementation of the chiral EP based on the proposed metasurface at  $\theta = \varphi = 45^\circ$  and wavelength of 1310 nm. a) Simulated phase and amplitude of reflection coefficients  $r_{-+}$  and  $r_{+-}$  in the parameter space ( $l_1, l_2$ ). b) The wavelength-dependent variation of the amplitude of reflection coefficients at  $(l_1, l_2) = (520, 175)$  nm. c) Real (up) and imaginary (down) parts of the corresponding reflection matrix eigenvalues  $\lambda_1$  and  $\lambda_2$ . d) Position of the two eigenstates (Es1 and Es2) on the Poincaré sphere as a function of wavelength, which is overlapped and degenerated into LCP at the south pole.

Here,  $r_{++}$  and  $r_{--}$  represent spin-preserved components, while  $r_{-+}$  and  $r_{+-}$  are spin-flipped components. The eigenvalues of the reflection matrix then can be derived as:

$$\lambda_{1,2} = \frac{(r_{++} + r_{--} \pm \sqrt{(r_{++} - r_{--})^2 + 4r_{-+}r_{+-}})}{2} \quad (3)$$

The optical reciprocity implies that  $r_{ps} = r_{sp}$ .<sup>[42–44]</sup> Using Equations (2) and (3), we can find that  $r_{++} = r_{--}$ , and the eigenvalues of  $\mathbf{R}_{\text{circ}}$  are degenerate when  $r_{-+}r_{+-} = 0$ . Thus, the chiral EPs of the reflection matrix  $\mathbf{R}_{\text{circ}}$  can be obtained by setting  $r_{-+}$  or  $r_{+-}$  to zero. For the proposed design,  $r_{-+}$  or  $r_{+-}$  can be optimized to zero in the parameter space consisting of  $l_1$  and  $l_2$  at a fixed operational wavelength and a desired incident angle. The control of  $r_{-+}$  or  $r_{+-}$  is attributed to the effective manipulation of the interference of GMRs in the designed metasurface, which is excited by two orthogonal linear polarization components of circularly polarized waves, as illustrated in Figure 1.

To quantitatively describe the performance of the designed metasurface, we numerically validate the realization of a chiral EP at a given incident angle ( $\theta = \varphi = 45^\circ$ ) and an operational wavelength of 1310 nm. Figure 2a shows the simulated amplitude and phase of reflection coefficients  $r_{-+}$  and  $r_{+-}$  of the designed metasurface in the parameter space defined by the

structural parameters  $l_1 \in [515, 525]$  nm and  $l_2 \in [170, 180]$  nm. Results indicate that the amplitude of  $r_{-+}$  exhibits a significantly large value, and the amplitude and phase of  $r_{+-}$  remain unchanged despite variations in  $l_1$  and  $l_2$ . On the contrary, the amplitude of  $r_{+-}$  is nearly zero at the point  $(l_1, l_2) = (520$  nm, 175 nm). A full  $2\pi$  reflection phase accumulation is obtained by encircling this point, thereby confirming the presence of a chiral EP. We further simulated the amplitude spectra of the four reflection coefficients in the reflection matrix of the designed metasurface at this point, as shown in Figure 2b. The amplitudes of reflection coefficients are expressed on a logarithmic scale ( $-20 \log(|r_{ij}|)$  dB). The amplitude of  $r_{+-}$  is lower than  $-60$  dB at 1310 nm, while the amplitudes of the remaining three reflection coefficients exhibit significantly higher values. These results suggest that the eigenvalues of the reflection matrix of the designed metasurface are degenerated into left-handed circularly polarized (LCP) light at 1310 nm. To make a validation, we examined the degeneracy of the eigenvalues and the corresponding eigenstates of the reflection matrix of the designed metasurface, as shown in Figure 2c,d. The evolution trajectories of the real and imaginary parts of the eigenvalues are shown in Figure 2c, exhibiting a crossing phenomenon as they traverse the chiral EP at 1310 nm. Correspondingly, the wavelength-dependent variation of the two eigenstates is mapped on the Poincaré sphere, as shown in Figure 2d. When the wavelength approaches 1310 nm, the two polarization

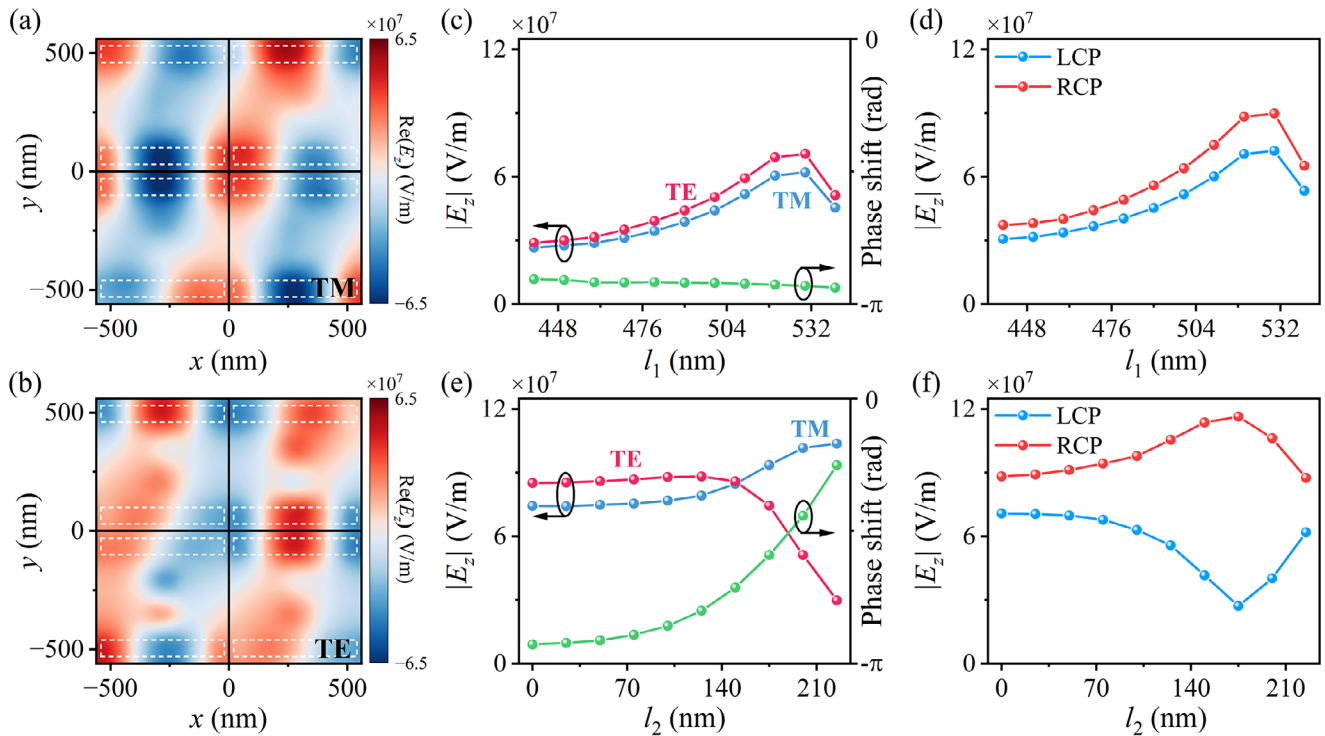


**Figure 3.** Modulation of the collective interference of GMRs. Simulated real part distribution of  $E_z$  at the middle plane of  $\text{SiO}_2$  layer for the designed metasurface without the short nanorod under a) TM and b) TE illuminations. Average amplitude and phase difference of  $E_z$  as a function of  $l_1$  or  $l_2$  under TM/TE and LCP/RCP illuminations c,d) without and e,f) with the short nanorod.

eigenstates gradually move toward the south pole and eventually degenerate into the LCP state. In other words,  $\mathbf{R}_{\text{circ}}|-\rangle = \lambda_{1,2}|-\rangle$ , and  $\lambda_1 = \lambda_2$  are two equivalent eigenvalues. These results provide convincing evidence for the achievement of the chiral EP at the given incident angle and operational wavelength based on the designed polyatomic metasurface. Note that, if the values of spin-preserved components ( $r_{++}$  and  $r_{--}$ ) approach zero, the designed metasurface acts as an external chiral mirror that perfectly absorbs optical waves of one spin state, while reflecting optical waves with the other spin state accompanied by spin flipping.<sup>[36,37]</sup>

The successful implementation of chiral EP can be achieved through the efficient manipulation of the collective interference between two GMRs, which are excited by the orthogonal linearly polarized components (TM and TE) of circularly polarized incident waves. It has been observed that the length  $l_2$  of the short nanorod plays a dominant role in controlling the collective interference between these two GMRs, as validated by the results in **Figure 3**. We first analyze the GMRs in the designed metasurface with the removal of short nanorods from its unit cell. As illustrated in **Figure 3a,b**, the presence of the long nanorods within the unit cell leads to the emergence of two GMRs that can be excited by TM and TE illuminations at the given incident angle and operational wavelength. The electric field distributions associated with the two GMRs exhibit similar characteristics, while the phase difference between them is nearly  $\pi$ . The resonant strength of the two GMRs can be effectively modulated by adjusting the length  $l_1$  of the two long nanorods in each unit cell, while maintaining a constant phase difference between the two

GMRs, as shown in **Figure 3c**. The LCP and right-handed circularly polarized (RCP) waves consist of both TM and TE components, with a phase difference of  $\pm\pi/2$ . Therefore, the phase difference between the two GMRs under LCP and RCP illuminations  $\approx -3\pi/2$  and  $\approx -\pi/2$ , respectively. The resonance modes under LCP and RCP illuminations can be treated as a direct superposition of the two GMRs. As shown in **Figure 3d**, the average values of  $|E_z|$  under LCP and RCP incidence first increase and then decrease with the increment of  $l_1$ , which is the same as the variation trend of the resonant strength of the two GMRs. The resonant strength of these modes under LCP and RCP incidence is not strong enough, leading to non-zero amplitudes of the cross-polarized reflection coefficients  $r_{-+}$  and  $r_{+-}$ . By adding the short nanorod in each unit cell and adjusting its length  $l_2$ , not only the resonant strength of the two GMRs can be significantly altered, but also their phase difference can be effectively manipulated, as shown in **Figure 3e**. When  $l_2$  changes from 100 to 220 nm, the averaged phase difference of  $E_z$  is approximately modulated from  $-0.9\pi$  to  $-0.3\pi$ . As shown in **Figure 3f**, for  $l_2 = 175$  nm, the two GMRs can exhibit destructive and constructive interference when illuminated with LCP and RCP waves, respectively. The constructive interference between the two GMRs leads to an increase in  $|E_z|$ , which indicates that the resonant strength increases and the absorption of the incident wave is enhanced. Therefore, the amplitude of  $r_{+-}$  is almost negligible. These results show that the realization of the chiral EP is attributed to the constructive interference between the two GMRs excited by TM and TE illuminations. This physical mechanism is quite different from the previous approaches, in which the

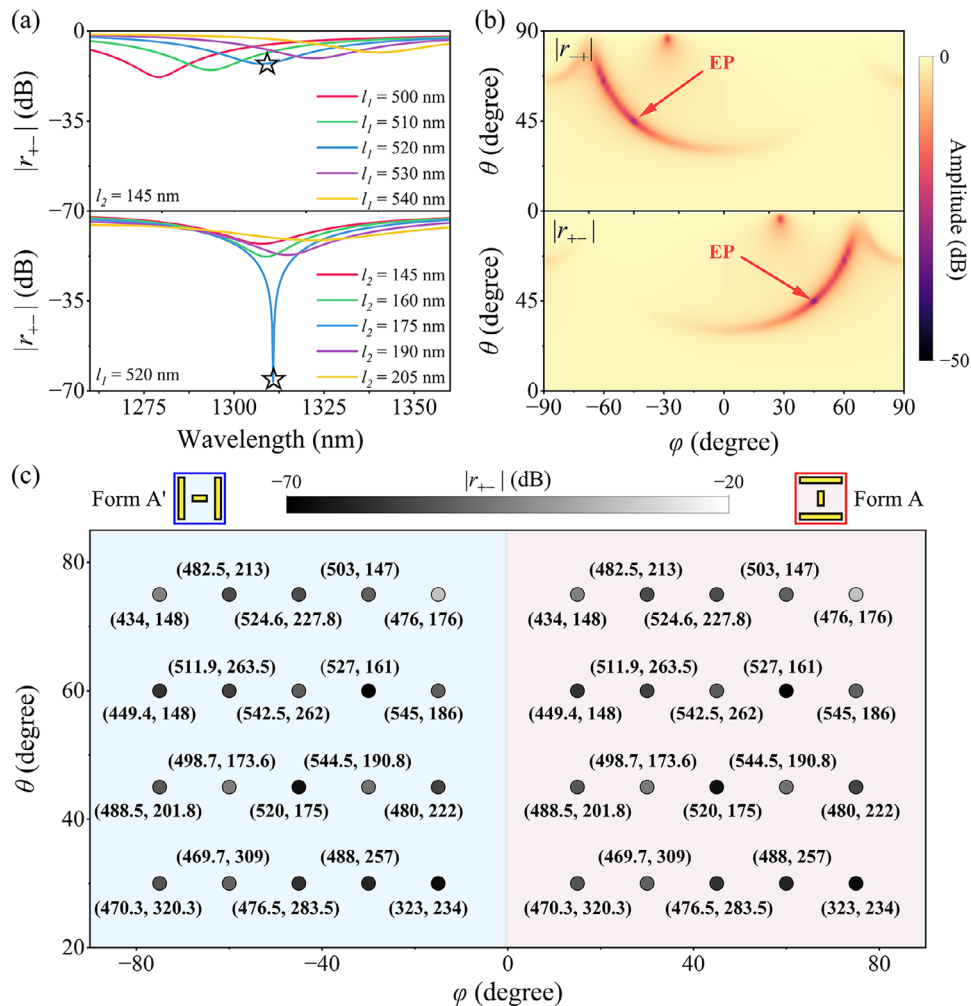


**Figure 4.** Manipulation of chiral EP in a wide-range momentum space at 1310 nm. a) Simulated amplitude spectra of  $r_{+-}$  at  $\theta = \varphi = 45^\circ$  with different  $l_1$  (up) and  $l_2$  (down). b) Simulated amplitude of  $r_{+-}$  and  $r_{-+}$  with various incident angles. The chiral EPs with opposite chirality appear at the two darkest points. c) Implementation of chiral EPs at 1310 nm in a wide-range momentum space by selecting the proper parameter space ( $l_1$ ,  $l_2$ ) in nanometers and structure (Form A and Form A').

chiral EPs were obtained based on the coupling between different resonators.<sup>[29,41]</sup>

The above discussion is conducted for the fixed incident angle and operational wavelength. It should be noted that both the incident angle and the operational wavelength are adjustable by changing  $l_1$  and  $l_2$  simultaneously. To investigate the dependence of reflection coefficient  $r_{+-}$  on  $l_1$  and  $l_2$ , we simulated the amplitude spectra of  $r_{+-}$  with the variation of  $l_1$  and  $l_2$  at  $\theta = \varphi = 45^\circ$ , as shown in **Figure 4a**. The operational wavelength of chiral EPs can be primarily determined by adjusting  $l_1$ , while the value of  $|r_{+-}|$  undergoes progressive changes as  $l_1$  is varied. The achievement of a chiral EP at the designated operational wavelength can then be realized by adjusting the amplitude of  $r_{+-}$  through varying  $l_2$ . Therefore, the chiral EPs with  $|r_{+-}| = 0$  can be achieved by sequentially adjusting  $l_1$  and  $l_2$  for the designated incident angles and operational wavelengths. Note that, the operational wavelength of chiral EP can only be adjusted around 1300 nm by varying  $l_1$  due to the limited adjustment range of  $l_1$  and the fact that the GMR is primarily influenced by the period of a unit cell

and the thickness of the SiO<sub>2</sub> interlayer; however, a broader range of modulation in the operational wavelength can be achieved by adjusting these structural parameters. The limited adjustment range of  $l_1$  and  $l_2$  also constrains the realization of chiral EPs in momentum space. Therefore, additional adjustments to the orientation angle of the unit cell are necessary to achieve chiral EPs that exhibit identical eigenstates across a wide range of momentum space. The designed structure exhibits mirror symmetry ( $M_{xz}$  and  $M_{yz}$ ) with respect to the  $x$ - $z$  and  $y$ - $z$  planes, while the LCP and RCP lights possess mutual mirror symmetry. Consequently, in momentum space, the chiral EPs invariably manifest as two pairs.<sup>[45,46]</sup> Specifically, if a chiral EP is realized at  $(\theta, \varphi)$ , an identical chiral EP can be found at  $(\theta, 180+\varphi)$ , while chiral EPs with opposite sign can be observed at  $(\theta, -\varphi)$  and  $(\theta, 180-\varphi)$ . For example, a chiral EP with  $|r_{+-}| = 0$  can be realized under  $\theta = \varphi = 45^\circ$  at 1310 nm. Correspondingly, another chiral EP with  $|r_{+-}| = 0$  can be observed under  $\theta = 45^\circ$ ,  $\varphi = -45^\circ$  at the same operational wavelength, as depicted in **Figure 4b**. Moreover, by simply rotating the structures in the unit cells by  $90^\circ$ , the chiral EP at

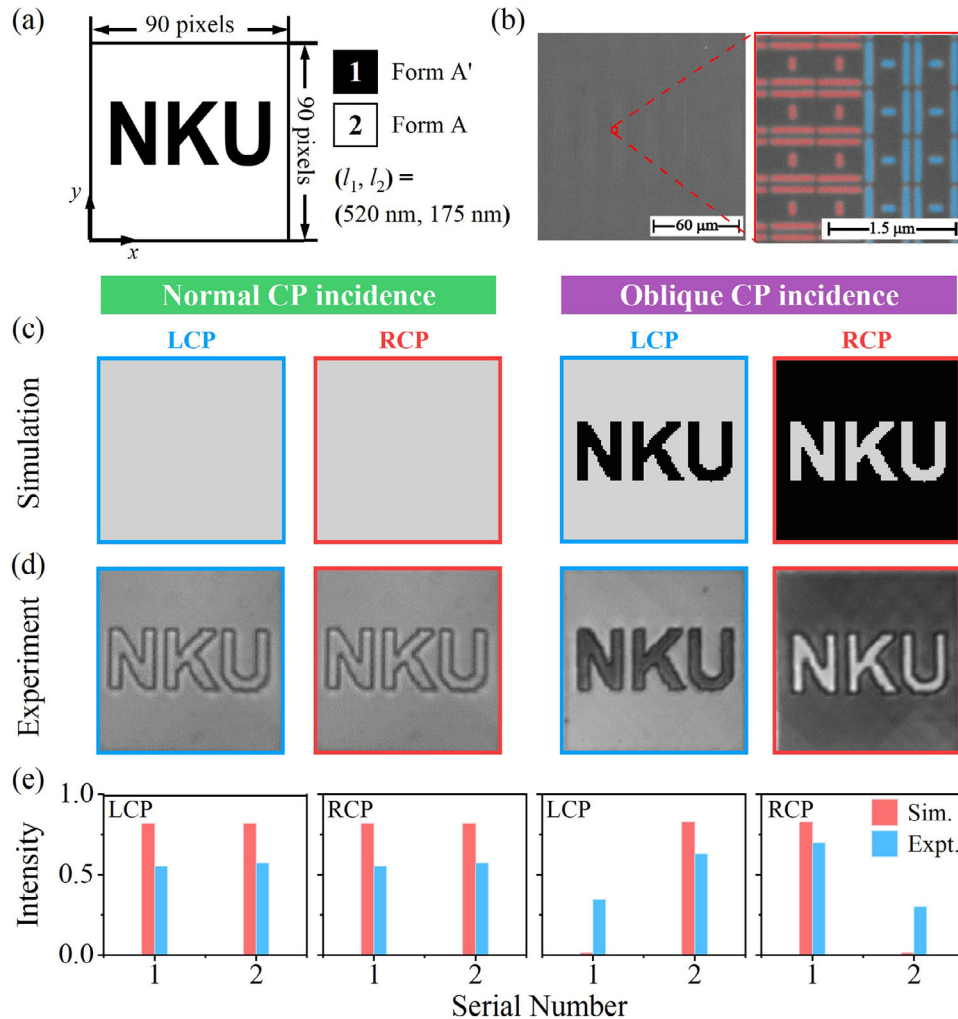


**Figure 5.** Realization of wavevector-selective two-level grayscale image. a) Schematic diagram of the designed two-level grayscale image, where the interior and exterior areas of “NKU” are composed of Form A’ and Form A, respectively. b) SEM images of the fabricated sample. c) Simulated and d) measured results of the designed grayscale image under normal and oblique ( $\theta = \varphi = 45^\circ$ ) incidences of the LCP and RCP. e) Simulated and measured the average reflection intensity of the two areas of the designed image.

( $\theta, 180+\varphi$ ) can be modulated to ( $\theta, 90-\varphi$ ),<sup>[42]</sup> providing a simple approach to realize chiral EPs with the same eigenstate in a wide-range momentum space. As an example, we realize chiral EPs with  $|r_{+-}| = 0$  in a wide-range momentum space ( $\theta \in [30^\circ, 75^\circ]$ ,  $\varphi \in [\pm 15^\circ, \pm 75^\circ]$ ) at 1310 nm by changing ( $l_1, l_2$ ) and rotating the unit cells by  $90^\circ$ , as shown in Figure 4c. The unit cell used here includes two forms: Form A’ with an orientation angle of  $90^\circ$  and Form A with an orientation angle of  $0^\circ$ . The orientation angle refers to the angle between the long axis of the short nanorods and the  $y$ -axis. The results suggest that within a broad momentum space range, chiral EPs with  $|r_{+-}|$  or  $|r_{-+}|$  equal to zero can be achieved by simply adjusting the orientation angle of the unit cell and the lengths of the nanorods, while the operational wavelength can be fixed.

The designed metasurface with chiral EPs is a good candidate for wavevector-selective gray imaging and optical encryption, since the reflection intensity at a given incident angle and a desired operational wavelength can be easily manipulated. To make

an experimental validation, we designed a two-level grayscale image of “NKU” composed of the two unit cells (Forms A’ and A) with ( $l_1, l_2$ ) = (520 nm, 175 nm), as illustrated in Figure 5a. The designed image has dimensions of  $90 \times 90$  pixels, with each pixel comprising  $3 \times 3$  identical unit cells. Figure 5b shows the scanning electron microscopy (SEM) image of the top view of the fabricated sample. Consistent with the design, the fabricated pattern is divided into interior and exterior areas, comprising Form A’ and Form A respectively. The “NKU” pattern is designed to be observed at  $\theta = \varphi = 45^\circ$  and 1310 nm. Due to the inevitable fabrication deviation of the fabricated sample, there is a red shift in the operational wavelength. The grayscale image was captured using an infrared charge-coupled device camera (CCD) in conjunction with a narrowband interference filter featuring a bandwidth of 12 nm (centered at 1320 nm). The simulated and experimental results of the two-level grayscale image under circularly polarized illumination are shown in Figure 5c,d), respectively. Due to that the unit cells (Form A’ and Form A) have reflection

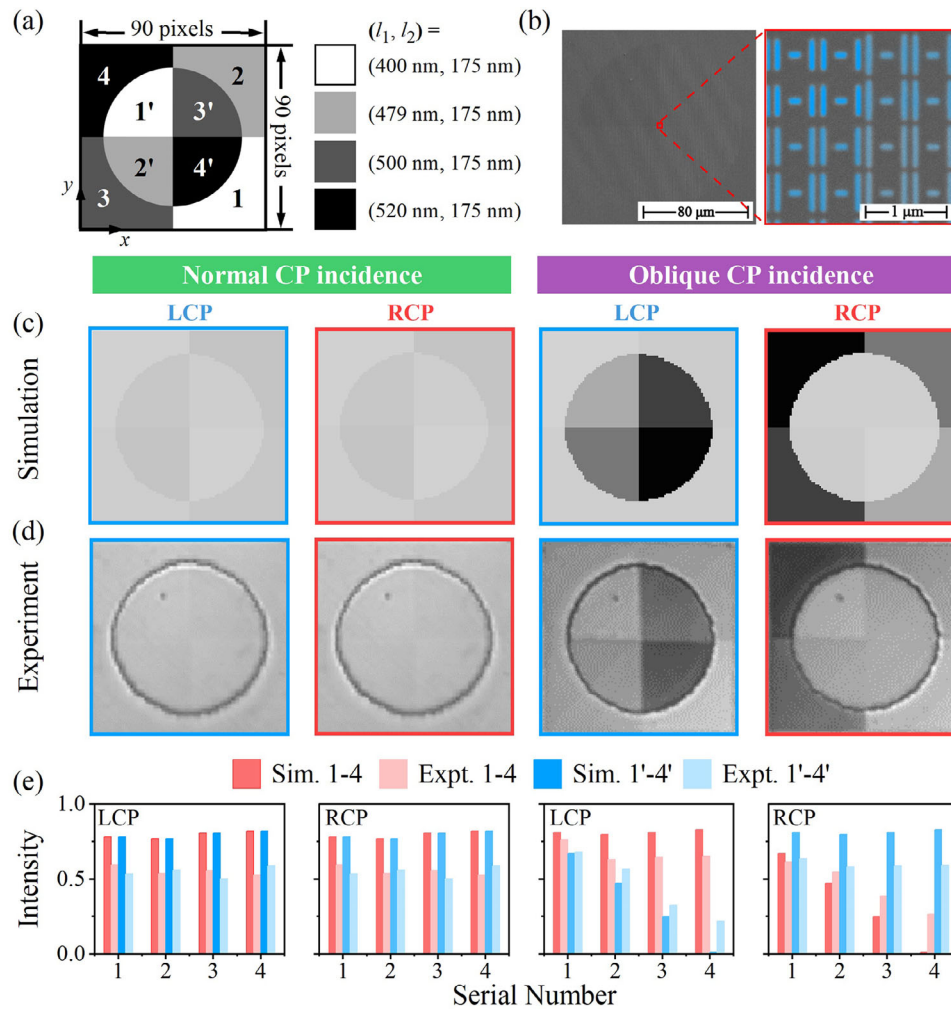


**Figure 6.** Realization of spin- and wavevector-selective four-level grayscale image. a) Schematic diagram of the designed spin-selective four-level grayscale image, in which the interior and exterior areas of the “circle” are composed of Form A’ and Form A with different parameters  $(l_1, l_2)$ , respectively. b) SEM images of the fabricated sample. c) Simulated and d) measured results of the designed grayscale image under normal and oblique ( $\theta = \varphi = 45^\circ$ ) incidences of the LCP and RCP. e) Simulated and measured the average reflection intensity of the eight segments of the designed image.

symmetry with respect to both the  $x$ - $z$  and  $y$ - $z$  planes, the reflection intensities of these two types of unit cells are equivalent under normal incidence. As a result, the grayscale image of “NKU” should not be observed under normal incidence. However, owing to the abrupt change of the orientation angles of the unit cells between the interior and exterior areas, a significant scattering of incident waves occurs at the junction, resulting in the observation of an outline of “NKU” in experimental results. Meanwhile, for oblique incidence with  $\theta = \varphi = 45^\circ$ ,  $|r_{+-}|$  of Form A is close to zero because of the existence of a chiral EP, while its  $|r_{-+}|$  is much larger, as verified by the results in Figure 2. On the contrary,  $|r_{-+}|$  of Form A’, which is equal to  $|r_{+-}|$  of Form A, is close to zero around the operational wavelength; and  $|r_{+-}|$  of Form A’, which is equal to  $|r_{-+}|$  of Form A, is much larger. Consequently, the Form A’ and Form A can be regarded as the fundamental elements representing “0” and “1” for 2-bit grayscale imaging when subjected to oblique LCP illumination. The simulated and measured results of the designed gray image under oblique LCP illumination are in good agreement with each other, thereby val-

idating the efficacy of the designed metasurface for achieving wavevector-selective gray imaging. The intensity distribution is reversed under oblique RCP illumination, as Form A’ and Form A can now be regarded as the fundamental elements representing “1” and “0” for 2-bit grayscale imaging. It is worth noting that the gray images under oblique illumination were obtained by clustering and integrating the multiple shots at different focal plane positions due to the constraint on the focal depth of the objective. To make a quantitative analysis between the simulated and experimentally measured gray images, we calculated the average intensity of the interior and exterior areas of the designed sample, as presented in Figure 5e. The simulated and measured results are in reasonable agreement with each other. The difference between the simulated and experimental results may be attributed to the fact that the simulation was performed for single-wavelength plane waves, while in the experiments, a microscope objective with a numerical aperture of 0.3 was used to focus the incident wave on the sample, and a narrow-band interference filter with a center wavelength of 1320 nm and full width half

maximum (FWHM) of 12 nm was used to control the spectral range of the incident wave. Meanwhile, the unavoidable fabrication deviation of the fabricated sample also affects the results. These results validate the applicability of metasurfaces consisting of these two types of unit cells (Form A' and Form A) with identical structural parameters for achieving wavevector-selective 2-level gray imaging.

Furthermore, high-level gray scale imaging and optical encryption can be realized by utilizing these two types of unit cells with different values of  $l_1$  and  $l_2$  since the reflection intensity at the given incident angle and operational wavelength can be effectively manipulated by changing  $l_1$  and  $l_2$ . A spin-selective 4-level grayscale image is designed to make an experimental validation, as shown in Figure 6a,b. The designed sample comprises 8 distinct areas, where areas 1 to 4 are composed of Form A with varying  $l_1$  and  $l_2$  while the areas 1' to 4' are composed of Form A' with different  $l_1$  and  $l_2$ . This sample was also designed to show the grayscale image under oblique circularly polarized incidence ( $\theta = \varphi = 45^\circ$ ) at the wavelength of 1310 nm. The areas with the same serial number, for example the areas 1 and 1', exhibit equivalent values of  $l_1$  and  $l_2$ , resulting in equal reflection intensity under oblique RCP and LCP illumination, respectively. The reflectance corresponding to the four grayscale levels is set as 0, 0.33, 0.66, and 1. Same as the previous sample, this sample is also composed of  $90 \times 90$  pixels, and each pixel consists of  $3 \times 3$  unit cells. The simulated and experimental results of the designed 4-level grayscale image under normal and oblique circularly polarized incidence are shown in Figure 6c,d, respectively, which are in good agreement with each other. For normal circularly polarized incidence, since the reflectance of the unit cells in the 8 areas of the designed sample is the same, the reflection intensity on the surface of the sample is uniform, rendering the grayscale image indiscernible. For oblique circularly polarized incidence, two distinct four-level grayscale images can be observed. Specifically, for oblique RCP incidence, the reflection intensities of the exterior areas (1 to 4) show a stepwise variation, while the reflection intensities of the interior areas (1' to 4') demonstrate minimal fluctuations. On the contrary, for oblique LCP incidence, the areas where the reflection intensity varies are reversed. The outline between the exterior and interior areas can still be observed in the experimental results. The four-level grayscale images cannot be identified under normal illumination, enabling the utilization of the designed metasurface for optical encryption. We further calculated the averaged reflectance of each area to quantitatively analyze the spin-selective reflection intensity distributions of the images in Figure 6c,d. The measured and simulated results are in reasonable agreement, and a stepwise variation of reflectance has been verified. These results demonstrated the applicability of our design for spin- and wavevector-selective multi-level grayscale imaging and optical encryption.

### 3. Conclusion

In summary, we have demonstrated an efficient approach for the manipulation of the chiral EP across a wide-range momentum space using a polyatomic metasurface. This approach distinguishes itself from other recently achieved chiral EPs by strategically modulating the collective interference of the GMRs excited under oblique TM and TE illuminations. Specifically, the con-

structive interference of the GMRs in the designed metasurface can be realized under oblique circularly polarized illumination by simply adjusting the structural parameters ( $l_1, l_2$ ), resulting in chiral EPs that can be manipulated across a wide momentum space while maintaining a fixed operational wavelength. We have theoretically and experimentally demonstrated the potential applications of our design in the spin- and wavevector-selective manipulation of reflection intensity, as well as optical encryption. Our results can further enrich the schemes for manipulating chiral EPs, offering valuable insights for the in-depth research of chiral EPs in momentum space.

### 4. Experimental Section

**Sample Fabrication:** The proposed polyatomic metasurfaces were fabricated by electron-beam lithography and gold lift-off processes. A 95 nm thick gold film was initially deposited onto a fused silica substrate by using an electron-beam evaporator. A 130 nm thick  $\text{SiO}_2$  layer was subsequently deposited onto the sample by using plasma-enhanced chemical vapor deposition. Then, a layer of poly (methyl methacrylate) (PMMA) electron resist with a thickness of 120 nm was spun on the  $\text{SiO}_2$  layer. To eliminate the charging effect on the dielectric substrate during the EBL process, which employs a 100 kV accelerating voltage and  $1000 \mu\text{C cm}^{-2}$  dose, a layer of poly (3,4-ethylenedioxythiophene) polystyrene sulfonate (PEDOT:PSS) with a thickness of 35 nm was spun-coated. After defining the patterns of designed nanostructure arrays by the EBL process, the PEDOT: PSS layer was removed with pure water for 60 s and PMMA was developed with methyl isobutyl ketone (MIBK)/isopropyl alcohol (IPA) (1:3) for 40 s. After that, a 30 nm thick gold layer was deposited by utilizing electron beam evaporation deposition. During the final lift-off procedure, the PMMA was removed with hot acetone at  $60^\circ\text{C}$  for 20 mins, remaining the polyatomic metasurfaces. Finally, a 126 nm thick layer of the SU-8 photoresist was then spin-coated onto the sample and UV-cured.

**Optical Measurement:** The experimental measurement of the proposed polyatomic metasurface for normal and oblique incidence was based on the custom-built setup. For the measurement of the gray images under normal incidence, a bromine tungsten lamp (Zolix, LSH-150) was used as the light source, and the light beam was collimated by a fiber collimator. The collimated beam passed through a broadband linear polarizer (IR 1300 BC5, Codixx AG) and a broadband quarter-waveplate ( $\lambda/4$  super achromatic waveplates, B. Halle Nachfl) to generate the circularly polarized incident beam. The circularly polarized beam then passed through a broadband unpolarized beam splitting prism (MFOPT, OQNP25.4N-NIR-3) and was focused on the sample with an objective (Sigma NIR plan apo 10x, NA = 0.3). The collected reflection beam passed through the unpolarized beam-splitting prism, and was collected by an InGaAs camera (HAMAMATSU InGaAs C10633). The gray images were acquired by the camera software. To capture the gray images at the operational wavelength (1320 nm), a narrowband filter (FB1320-12, THOLABS) was employed. The gray images under oblique incidence ( $\theta = \varphi = 45^\circ$ ) were measured with the incident path and reflected path being mutually perpendicular. Compared to the measurement under normal incident conditions, the difference is that the sample was rotated with respect to the plane perpendicular to the direction of beam propagation. Another objective (Sigma NIR plan apo 20x, NA = 0.45) was used in the reflected path to collect the reflected light from the sample.

**Numerical Simulation:** The numerical simulations were performed by using the finite differential time domain methods. The refractive index of  $\text{SiO}_2$  and SU-8 was set to be 1.47 and 1.57, respectively. The permittivity of Au was obtained from Johnson and Christy.<sup>[47]</sup> The periodic boundary conditions were set in the  $x$  and  $y$  directions representing a periodical structure, and waveguide ports boundary was defined in the  $z$  direction for light incidence while the excitation source was either a left- or a right-handed circularly polarized plane wave. At least 15 mesh steps per wavelength were used to ensure the accuracy of the calculated results.

## Acknowledgements

This work was supported by the National Key Research and Development Program of China (Nos. 2021YFA1400601 and 2022YFA1404501), the National Natural Science Fund for Distinguished Young Scholars (No. 11925403), the National Natural Science Foundation of China (Nos. 12122406, 12192253, 12274237, 12274239, and U22A20258), and the Natural Science Foundation of Tianjin (Nos. 22JCYBJC01350, 22JCZDJC00400 and 22JCYBJC00800).

## Conflict of Interest

The authors declare no conflict of interest.

## Data Availability Statement

The data that support the findings of this study are available from the corresponding author upon reasonable request.

## Keywords

chiral exceptional points, guided-mode interference, optical encryption, optical intensity manipulation, polyatomic metasurface

Received: November 30, 2023

Revised: February 18, 2024

Published online:

- [1] C. M. Bender, S. Boettcher, *Phys. Rev. Lett.* **1988**, *80*, 5243.
- [2] M.-A. Miri, A. Alù, *Science* **2019**, *363*, eaar7709.
- [3] W. D. Heiss, *J Phys A Math Gen* **2004**, *37*, 2455.
- [4] Y. Ashida, Z. Gong, M. Ueda, *Adv. Phys.* **2020**, *69*, 249.
- [5] L. J. Xu, G. L. Dai, G. Wang, J. P. Huang, *Phys. Rev. E* **2020**, *102*, 032140.
- [6] H.-Z. Chen, T. Liu, H.-Y. Luan, R.-J. Liu, X.-Y. Wang, X.-F. Zhu, Y.-B. Li, Z.-M. Gu, S.-J. Liang, H. Gao, L. Lu, L. Ge, S. Zhang, J. Zhu, R.-M. Ma, *Nat. Phys.* **2020**, *16*, 571.
- [7] T. Gao, G. Li, E. Estrecho, T. C. H. Liew, D. Comber-Todd, A. Nalitov, M. Steger, K. West, L. Pfeiffer, D. W. Snoke, A. V. Kavokin, A. G. Truscott, E. A. Ostrovskaya, *Phys. Rev. Lett.* **2018**, *120*, 065301.
- [8] I. Carusotto, C. Ciuti, *Rev. Mod. Phys.* **2013**, *85*, 299.
- [9] K. Ding, G. Ma, M. Xiao, Z. Zhang, C. T. Chan, *Phys. Rev. X* **2016**, *6*, 021007.
- [10] S.-B. Lee, J. Yang, S. Moon, S.-Y. Lee, J.-B. Shim, S. W. Kim, J.-H. Lee, K. An, *Phys. Rev. Lett.* **2009**, *103*, 134101.
- [11] W. Chen, Ş. Kaya Özdemir, G. Zhao, J. Wiersig, L. Yang, *Nature* **2017**, *548*, 192.
- [12] S. N. Ghosh, Y. D. Chong, *Sci. Rep.* **2016**, *6*, 19837.
- [13] M. Y. Nada, M. A. K. Othman, F. Capolino, *Phys. Rev. B* **2017**, *96*, 184304.
- [14] D. A. Bykov, L. L. Doskolovich, *Phys. Rev. A* **2018**, *97*, 013846.
- [15] T. Wu, W. Zhang, H. Zhang, S. Hou, G. Chen, R. Liu, C. Lu, J. Li, R. Wang, P. Duan, J. Li, B. Wang, L. Shi, J. Zi, X. Zhang, *Phys. Rev. Lett.* **2020**, *124*, 083901.
- [16] A. Regensburger, M.-A. Miri, C. Bersch, J. Näger, G. Onishchukov, D. N. Christodoulides, U. Peschel, *Phys. Rev. Lett.* **2013**, *110*, 223902.
- [17] X. Jiang, L. Yang, *Light Sci Appl* **2020**, *9*, 24.
- [18] H. Nasari, G. Lopez-Galmiche, H. E. Lopez-Aviles, A. Schumer, A. U. Hassan, Q. Zhong, S. Rotter, P. LiKamWa, D. N. Christodoulides, M. Khajavikhan, *Nature* **2022**, *605*, 256.
- [19] X. Yin, X. Zhang, *Nat. Mater.* **2013**, *12*, 175.
- [20] Y. Huang, Y. Shen, C. Min, S. Fan, G. Veronis, *Nanophotonics* **2017**, *6*, 977.
- [21] J. Doppler, A. A. Mailybaev, J. Böhm, U. Kuhl, A. Girschik, F. Libisch, T. J. Milburn, P. Rabl, N. Moiseyev, S. Rotter, *Nature* **2016**, *537*, 76.
- [22] H. Xu, D. Mason, L. Jiang, J. G. E. Harris, *Nature* **2016**, *537*, 80.
- [23] H. Zhou, C. Peng, Y. Yoon, C. W. Hsu, K. A. Nelson, L. Fu, J. D. Joannopoulos, M. Soljačić, B. Zhen, *Science* **2018**, *359*, 1009.
- [24] S. Longhi, L. Feng, *Photonics Res* **2017**, *5*, B1.
- [25] H. Hodaie, M. A. Miri, A. U. Hassan, W. E. Hayenga, M. Heinrich, D. N. Christodoulides, M. Khajavikhan, *Opt. Lett.* **2015**, *40*, 4955.
- [26] A. Guo, G. J. Salamo, D. Duchesne, R. Morandotti, M. Volatier-Ravat, V. Aimez, G. A. Siviloglou, D. N. Christodoulides, *Phys. Rev. Lett.* **2009**, *103*, 093902.
- [27] Y. Zhao, A. Alù, *Phys. Rev. B* **2011**, *84*, 205428.
- [28] S. H. Park, S.-G. Lee, S. Baek, T. Ha, S. Lee, B. Min, S. Zhang, M. Lawrence, T.-T. Kim, *Nanophotonics* **2020**, *9*, 1031.
- [29] M. Kang, J. Chen, Y. D. Chong, *Phys. Rev. A* **2016**, *94*, 033834.
- [30] S. Yu, H. S. Park, X. Piao, B. Min, N. Park, *Optica* **2016**, *3*, 1025.
- [31] A. Krasnok, D. Baranov, H. Li, M.-A. Miri, F. Monticone, A. Alù, *Adv. Opt. Photonics* **2019**, *11*, 892.
- [32] T. Wu, W. Zhang, H. Zhang, S. Hou, G. Chen, R. Liu, C. Lu, J. Li, Wang, R., P. Duan, J. Li, B. Wang, L. Shi, J. Zi, X. Zhang, *Phys. Rev. Lett.* **2020**, *124*, 083901.
- [33] C. Wang, W. R. Sweeney, A. D. Stone, L. Yang, *Science* **2021**, *373*, 1261.
- [34] H. Yin, R. Bai, X. Gu, C. Zhang, G. R. Gu, Y. Q. Zhang, X. R. Jin, Y. Lee, *Opt. Commun.* **2018**, *414*, 172.
- [35] X. Gu, R. Bai, C. Zhang, X. R. Jin, Y. Q. Zhang, S. Zhang, Y. P. Lee, *Opt. Express* **2017**, *25*, 11778.
- [36] E. Plum, N. Zheludev, *Appl. Phys. Lett.* **2015**, *106*, 221901.
- [37] Z. Li, W. Liu, H. Cheng, D. Choi, S. Chen, J. Tian, *Adv. Mater.* **2020**, *32*, 1907983.
- [38] Z. Li, H. Cheng, S. Chen, *Sci China Phys Mech Astron* **2021**, *64*, 264231.
- [39] S. Yu, J. Cheng, Z. Li, W. Liu, H. Cheng, J. Tian, S. Chen, *ChemPhys-Mater* **2022**, *1*, 6.
- [40] S. Baek, S. H. Park, D. Oh, K. Lee, S. Lee, H. Lim, T. Ha, H. S. Park, S. Zhang, L. Yang, B. Min, T.-T. Kim, *Light Sci Appl* **2023**, *12*, 87.
- [41] Q. Song, M. Odeh, J. Zúñiga-Pérez, B. Kanté, P. Genevet, *Science* **2021**, *373*, 1133.
- [42] V. Dmitriev, I. E. E. E. Trans, *Antennas Propag* **2013**, *61*, 185.
- [43] R. Bhandari, *JOSA A* **2009**, *26*, 2368.
- [44] J. Li, J. Fu, Q. Liao, S. Ke, *JOSA B* **2019**, *9*, 36.
- [45] S. Zanolto, G. Mazzamuto, F. Riboli, G. Biasiol, G. C. La Rocca, A. Tredicucci, A. Pitanti, *Nanophotonics* **2019**, *8*, 2291.
- [46] R. Singh, E. Plum, W. Zhang, N. I. Zheludev, *Opt. Express* **2012**, *18*, 13425.
- [47] P. B. Johnson, R. W. Christy, *Phys. Rev. B* **1972**, *6*, 4370.